scientific reports

Check for updates

OPEN

Influence of phonon anharmonicity on Raman spectra of $Cu_2ZnSn(S,Se)_4$ polycrystalline thin films through computational study

Yurii A. Romaniuk[1,2]✉, Ivan S. Babichuk[2,3]✉, Vadym V. Korotyeyev[2], Volodymyr O. Yukhymchuk[2], Volodymyr M. Dzhagan[2], Sergiy V. Virko[2], Mykola O. Semenenko[2], Maksym O. Stetsenko[4,5], Anton Tiutiunnyk[6]✉, Laura M. Pérez[7] & David Laroze[8]

$Cu_2ZnSn(S,Se)_4$ (CZT(S,Se)) thin films exhibit the characteristics necessary to be effective absorbers in solar cells. In this report, the room temperature experimental Raman scattering spectra, recorded at different excitation wavelengths, are systematically analyzed theoretically using the results of DFT harmonic frequencies calculations at the *Γ*-point for various modifications of kesterite (KS), stannite (ST), and pre-mixed Cu-Au (PMCA) crystal structures. The specific anharmonism-induced features in the spectra of CZT(S,Se) crystals are identified, and the spectral lineshapes at varied strengths of anharmonic interaction are simulated. A robust agreement between the experimental Raman spectrum and the theoretical results is demonstrated, ensuring the reliability of estimating parameters related to anharmonic effects. Therefore, our findings show that incorporating anharmonism as an additional contribution to the phonon spectra, particularly in non-resonant cases, allows for a more accurate description of the vibrational properties of CZT(S,Se). This could play a crucial role in distinguishing between different phases of CZT(S,Se) materials and open new possibilities for the fabrication of solar cells with enhanced characteristics.

Keywords CZT(S,Se), Kesterite, Fermi resonance, Raman spectra, Anharmonicity, DFT calculation

Copper zinc tin sulfide (Cu_2ZnSnS_4, CZTS), copper zinc tin selenide ($Cu_2ZnSnSe_4$, CZTSe), and their alloys ($Cu_2ZnSnS_{4(1-x)}Se_{4x}$, where $0<x<1$, CZTSSe) are promising materials for solar cells due to their suitable direct band gaps (1.45 eV for CZTS and 1.0 eV for CZTSe), high absorption coefficients ($<10^4$ cm^{-1}), and the abundance of constituent materials of Earth's surface[1–7]. However, kesterite solar cells still have a certified efficiency of about 13.8%,[8] which is far from the theoretical maximum of 32.2% (Shockley-Queisser limit)[9–11]. This efficiency gap is largely due to the open-circuit voltage deficit and structural variability during film growth, making theoretical and computational methods vital for addressing these challenges[12–15]. Therefore, despite the outstanding properties of these semiconductors, solar cells based on them are still in the process of improvement.

Nowadays, Raman spectroscopy is an essential tool for analyzing the quality of CZTS and CZTSe by detecting deviations in crystal symmetry, which indicates lattice disorder that limits the efficiency of solar cells[16–18]. Altosaar et al.[19] conducted a pioneering study on phonon spectra in CZTS and CZTSe using Raman scattering. Furthermore, several studies[20–22] have used Density Functional Theory (DFT) to model lattice dynamics in kesterite (KS), stannite (ST), and pre-mixed Cu-Au (PMCA) structures. In particular, Ref.[20] analyzed experimental Raman spectra[19] of CZTS and CZTSe, differentiating these structural forms by deconvoluting the spectra into

[1]State Key Laboratory of Precision Spectroscopy, East China Normal University, Shanghai 200241, People's Republic of China. [2]V. Ye Lashkaryov Institute of Semiconductor Physics, NAS of Ukraine, Kyiv 03680, Ukraine. [3]School of Mechanical and Automation Engineering and Jiangmen Key Laboratory of Intelligent Manufacturing of Polymer Materials, Wuyi University, Jiangmen 529020, People's Republic of China. [4]School of Science, Westlake University, Hangzhou 310024, Zhejiang, People's Republic of China. [5]Institute of Natural Sciences, Westlake University, Hangzhou 310024, Zhejiang, People's Republic of China. [6]Departamento de Física, FACI, Universidad de Tarapacá, 1000000 Arica, Chile. [7]Departamento de Ingeniería Industrial y de Sistemas, Universidad de Tarapacá, 1000000 Arica, Chile. [8]Instituto de Alta Investigación, Universidad de Tarapacá, 1000000 Arica, Chile. ✉email: yurii@lps.ecnu.edu.cn; romanyuk_yu@ukr.net; ivan@szu.edu.cn; tyutyunnyk.a.m@uta.cl

Lorentzian (or Gaussian) components and incorporating Γ-point frequencies from DFT. This approach linked specific Raman bands to distinct modifications (KS, ST, and PMCA), as demonstrated in Refs[20,22–26].

As is well known, vibrational anharmonicity in materials like CZTS and CZTSe can lead to deviations in energy levels, affecting charge transport and defect formation – two crucial factors influencing solar cell performance. Temperature-dependent anharmonicity significantly impacts Raman spectra, broadening peaks due to mode coupling and higher-order terms in the potential energy[27–30]. Such anharmonic effects can also induce phenomena like Fermi resonance (FR)[31,32], which modifies the intensity and frequency of Raman bands by mixing fundamental vibrations with overtones or combination tones. It is noteworthy that the authors of Refs[20,22–26], in their analysis of the Raman spectrum of CZTS and CZTSe, did not consider important features related to anharmonic effects, which can cause shifts in band positions and intermixing of different lattice excitations. This intermixing creates two bands of comparable intensity, known as the Fermi doublet. Originally observed in CO_2 molecules by E. Fermi[33], FR has since been identified in various molecules and crystals, including layered $ReSe_2$[34], 2D materials[35], bulk MoS_2[36], and semiconductors such as Si[30], SiO_2[37], GaP[38], and $AlPO_4$[38,39]. In addition, it has been demonstrated that crystals with multiple atoms in the unit cell, such as quaternary metal chalcogenides, exhibit the FR effect[31]. Notably, FR in crystals manifests in a rather complex form due to the dispersion of the phonon branch (e.g.,[32,40]) and is analogous to Fano resonance, arising between a discrete level and a continuum spectrum[41].

Thus, the precise nature of the influence of FR on CZT(S,Se) remains an open research question. Theoretical models and experimental Raman measurements are key tools for advancing our understanding of its effects. For practical applications, achieving high-quality, single-phase CZTS or CZTSe with a coherent crystal structure and stoichiometric elemental composition is crucial. Experimental techniques such as Raman spectroscopy, alongside computational methods like DFT, significantly enhance insights into vibrational characteristics and aid in phase identification with high accuracy. While DFT is a powerful tool, it is computationally intensive, making simpler theoretical approaches valuable for addressing FR challenges. Overall, exploring the role of FR in CZT(S,Se) through both theoretical models and experimental Raman measurements is essential, as it underscores the need for a detailed analysis of the material's vibrational properties, which influence photovoltaic performance and other applications.

Herein, we report the influence of anharmonism on the Raman spectra of CZTS and CZTSe polycrystalline thin films with different structures (KS, ST, and PMCA) at room temperature and non-resonant excitation. By employing Yaremko's theoretical approach[32,40], we derived anharmonic interaction parameters directly from experimental data through precise fitting of the Raman spectra. The fitting method is based on a simplified model in which a high-frequency fundamental vibration interacts with the first overtone of a low-frequency oscillator, with their frequencies differing by approximately a factor of two. The Green's function method was employed to derive theoretical relations for the light scattering intensity $I(\omega)$ under anharmonic interactions[32,42]. The following section outlines these relations, detailing how anharmonic intermixing between fundamental and second-order vibrations can produce distinctive features in Raman spectra near fundamental bands.

Results and discussion

CZTS polycrystalline thin film

The most intense bands observed in the experimental studies in the A (or A_1) representation have frequencies of $\omega_1 = 338$ cm^{-1} and $\omega_2 = 287$ cm^{-1} (Fig. 1). The observed spectrum in Ref.[20] was deconvoluted into several simple Gaussian bands, with each peak assigned to an individual (fundamental) Gaussian component. In our work, Lorentzian deconvolution was used (Fig. 1). Lorentzian profiles are particularly suited for interpreting phonon peaks, which typically exhibit well-defined widths and heights, thereby facilitating comparisons with theoretical calculations[43,44]. By fitting the experimental spectrum of the CZTS polycrystalline thin film in Fig. 1 with a set of Lorentzians, we determined that a weaker band exists at about 332 cm^{-1} on the low-frequency side of the most intense band at 338 cm^{-1}, and similarly, a weaker band at 285 cm^{-1} near the second intense band at 287 cm^{-1}.

For the 287 cm^{-1} band, the intensity of its low-frequency component (285 cm^{-1}) is quite weak, but its nature is analogous to that of the much stronger 332 cm^{-1} band. Therefore, the main discussion here will focus on the 338 cm^{-1} band. The authors in Refs.[45–50] proposed an approach for identifying the disordered kesterite phase from Raman spectra by detecting the amount of intrinsic structural defects, such as antisite Zn_{Cu} and V_{Cu}. The 332 cm^{-1} band was associated with these defects in the CZTS lattice. The degree of disorder in the CZTS structure was estimated from the intensity ratio between the disordered kesterite phase band at 332 cm^{-1} and the ordered one at 338 cm^{-1}, with $I_{332}/I_{338} = 0.087$. The CZTS film exhibits a low ratio compared to other reported results[51]. Additionally, the obtained results are consistent with the FWHM analysis of diffraction peaks (see Supplementary Information (SI), Fig. S1k online). This indicates a low content of the disordered kesterite phase. However, as shown in the present work, the spectral lineshape in the range of the strongest band at $\omega_1 = 338$ cm^{-1} (as well as the structure accompanying the $\omega_1 = 198$ cm^{-1} band in CZTSe) can be explained from another perspective, specifically due to anharmonic mixing of states. Below, we individually consider each of the three structures (KS, ST, and PMCA) of the CZTS polycrystalline thin film and estimate their contribution to the spectrum.

Kesterite (KS)

The space group of this structure is $I\overline{4}(S_4^2)$[28,52], and the point symmetry group is S_4. The irreducible representations of this group are shown for convenience in SI Table S1. According to group theory, for each finite-order group, the number of irreducible representations coincides with the number of classes, which, in this case, is equal to the number of the group elements $h = 4$. Therefore, one can readily obtain the characters (spurs) for the B^2 and $E^2_{1,2}$ representations by using Table S1 for the point group S_4. The results are presented in the

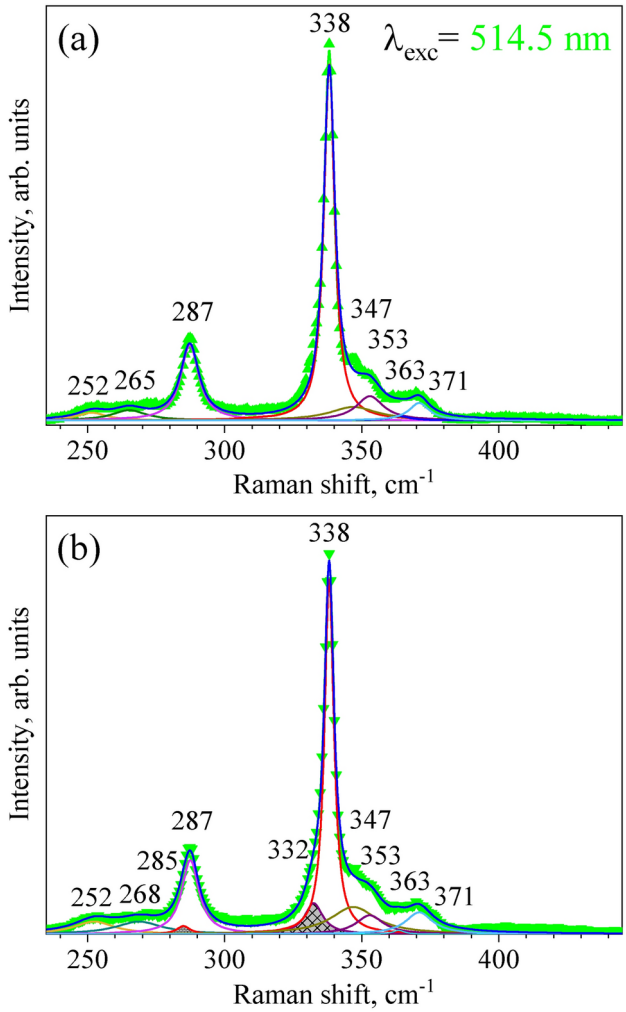

Fig. 1. Raman spectrum of a CZTS thin film at $\lambda_{ext} = 514.5$ nm (~ 2.41 eV) and room temperature. The green line (triangles) represents the sum of the peaks (blue) used to deconvolve the experimental spectrum: (**a**) each of the two most intense Raman scattering (RS) peaks at $\omega_1 = 338$ cm^{-1} and $\omega_2 = 287$ cm^{-1} is assumed, according to Ref.[20], to be due to the RS from the KS CZTS phase only; (**b**) the same peaks are assumed, according to Ref.[20] to consist of two closely spaced peaks from the KS ($\omega_1 = 338$ cm^{-1} and $\omega_2 = 287$ cm^{-1}) and the disordered KS phase, similar to the ST phases[45–51] ($\omega_1 = 332$ cm^{-1} and $\omega_1 = 285$ cm^{-1}).

last two lines of Table S1. It is important to note that both the E_1 and E_2 representations should be considered independent and non-degenerate.

The strongest bands in the Raman spectra correspond to A-symmetry. Therefore, only B^2 overtones (or combination tones) can be observed in the same A-symmetry, as shown in Table S1. Moreover, only these states can be intermixed and enhanced due to their interaction with the fundamental of A-symmetry, because the wave functions of the mixing states must have the same symmetry. For the KS structure, the DFT- calculated phonon frequencies for the A representation are $\widetilde{\omega}_1 = 340.04$ cm^{-1} and $\widetilde{\omega}_2 = 284.30$ cm^{-1}, as presented in Table 1. In our study, we also conducted independent phonon calculations using Density Functional Perturbation Theory (DFPT) within the Quantum ESPRESSO suite, with the aim of comparing our results with those reported in other references, as shown in Table 1. It should be noted that, as in Ref.[20], our current DFT calculation utilized the generalized gradient approximation (GGA) for the exchange–correlation functional, which typically provides higher accuracy for phonon frequencies compared to the local density approximation (LDA) (see Ref.[21]). Furthermore, we employed key parameter values similar to those in Refs.,[20,22] including the plane-wave cutoff energy, k-point sampling, and the choice of exchange–correlation functional and pseudopotentials, for our DFT calculations of phonon frequencies at the Γ- point. However, since we performed a full structural relaxation to accurately determine the equilibrium atomic positions, our calculated phonon frequencies may differ slightly from those reported in previous studies (see Table 1). This relaxation step is crucial, as even minor changes in atomic positions can influence the interatomic force constants and, consequently, the phonon frequencies. As a result, we obtained lattice parameters (see SI Table S2) with a deviation of less than 1% from the experimental values, providing a solid basis for precise phonon frequency calculations. However, consistent with previous DFT studies[21,23] a discrepancy was observed between the calculated Raman frequencies at the Γ-point and the

Kesterite				Stannite				PMCA				Experiment
Symmetry	Work[20]	Work[22]	This work	Symmetry	Work[20]	Work[22]	This work	Symmetry	Work[20]	Work[22]	This work	CZTS
	340.04	298.8	332.1	A_1	334.08	293.5	302.0	A_1	334.42	303.9	305.0	338
A	284.30	273.0	294.0		277.12	281.0	290.2		299.25	290.6	291.0	287
	272.82	270.0	273.6	A_2	263.11	269.3	279.2	A_2	266.13	263.1	263.6	268
	355.80	321.2	320.4	B_1	291.12	284.2	291.8	B_1	–			
	238.48	225.8	225.6		74.17	78.7	80.8					
B(TO)	166.65	159.4	162.0	B_2	277.08	275.0	282.4	B_2	278.85	270.6	268.7	252
	98.82	95.3	95.4		149.69	146.2	135.2		148.63	146.6	141.9	
	86.70	85.5	79.8		95.85	91.2	91.3		87.21	80.7	80.0	
E_1(TO)	351.10	306.8	306.3	E	264.37	269.7	269.5	E	277.85	272.4	273.8	353
	247.80	246.9	245.8		235.41	224.3	240.8		164.81	157.4	159.3	
E_2(TO)	150.0	144.3	148.4		161.68	152.0	162.4		86.29	87.8	88.8	
	102.9	95.0	99.0		97.34	97.6	106.0					

Table 1. The calculated Γ-point phonon frequencies (in cm^{-1}) for the KS, ST, and PMCA structures of CZTS in this work, along with those reported in Refs.[20,22], are compared with the experimental Raman frequencies of the polycrystalline thin film presented in this study.

corresponding experimental values. Therefore, it can be assumed that the discrepancy between the experiment and the DFT calculations is due to additional factors not considered in the numerical DFT calculations. One such factor could be anharmonic interactions between the vibrations, leading to a shift and mixing of phonons of different orders in the crystal. In the case of intermixing the fundamental mode with a weak overtone or a combination tone, two strong bands of comparable intensity can appear due to the FR phenomenon[27,31,35].

Moreover, due to phonon dispersion in the frequency range corresponding to the overtone (or the combination tone), a rather complicated structure can arise, depending on the phonon dispersion of the pair of modes forming the combination tone. In the KS structure, as shown in Table 1, which includes selected phonon frequency values from Ref.[20], there is no suitable combination tone of B-symmetry close to $\widetilde{\omega}_1 = 340.04$ cm^{-1}, except for a sum mode: $\widetilde{\omega}_a$(238.48 cm^{-1}) $+\widetilde{\omega}_b$(98.82 cm^{-1}) = 337.3 cm^{-1} (each B-symmetry). This combined mode is expected to shift upward due to its interaction with the fundamental band at $\widetilde{\omega}_1 = 340.04$ cm^{-1}. Therefore, this band should be observed experimentally at $\overline{\omega}_1 > 340.04$ cm^{-1}. On the other hand, there is also a suitable difference between fundamental frequencies: $\widetilde{\omega}_3$ (355 cm^{-1})$-\widetilde{\omega}_4$ (86.7 cm^{-1}) = 269.1 cm^{-1}, located somewhat lower than another fundamental band, $\widetilde{\omega}_2 = 284.30$ cm^{-1}. Due to the interaction between this combination pair $(\widetilde{\omega}_3 - \widetilde{\omega}_4)$ and $\widetilde{\omega}_2$, the fundamental band will be shifted upward. Hence, the calculated $\widetilde{\omega}_2$ can be experimentally observed at $\omega_2 =$ 287 cm^{-1}. This will be discussed in the subsequent section, analyzing the experimental data.

Stannite (ST) and PMCA

The space groups of these structures are $I\overline{4}2m(D_{2d}^{11})$[53] and $P\overline{4}2m(D_{2d}^{1})$[52], respectively, both of which are characterized by the same point group symmetry, D_{2d}. The irreducible representations of this point group are presented in SI Table S3. From Eq. (5), one can obtain the characters $\{\chi_E^2(g)\}_+$, as shown in the last line of Table S3, and using Eq. (6), we can derive all irreducible representations included in $\{\chi_E^2(g)\}_+$. The number of elements in this group is $h = 8$, and simple calculations lead to the following results: $r(A_1) = 1, r(A_2) = 0, r(E) = 0, r(B_1) = r(B_2) = 1$. It is important to note that a combination tone (or an overtone) of a doubly degenerate E-state can be observed in the A_1-symmetry. Moreover, it can interact with a fundamental A_1 vibration and, hence, should be enhanced if the energy difference between the two is small. This allows for the identification and study of acceptable pairs of E-states in Table 1 for the ST and PMCA structures. In the ST crystal structure, there are at least two combination tones of E-symmetry close to the fundamental frequency $\widetilde{\omega}_1 = 334.08$ cm^{-1}: $\widetilde{\omega}_5$ (264.37 cm^{-1}) $+\widetilde{\omega}_7$ (97.34 cm^{-1}) = 361.71 cm^{-1} and $\widetilde{\omega}_6$ (235.41 cm^{-1})$+\widetilde{\omega}_7$ (97.34 cm^{-1}) = 332.75 cm^{-1}. The second combination tone is very close to the fundamental band $\widetilde{\omega}_1$, but the interaction between them is weak. As a result, an upward shift of $\widetilde{\omega}_1$ by 3–4 cm^{-1} may occur (the magnitude is approximately estimated from the energy difference between the interacting states), so $\omega_1 \approx$ 338 cm^{-1}. The interaction with the other combination tone, $\widetilde{\omega}_5 + \widetilde{\omega}_7 \approx 362$ cm^{-1}, is clearly stronger, resulting in a more complex structure slightly above the fundamental ω_1 band (Fig. 7a in Ref.[20] or Fig. 1a in the present work). Additionally, the combination tone $\{B_2^2\}_+\widetilde{\omega}_8$ (277.08 cm^{-1})$+\widetilde{\omega}_9$ (95.85 cm^{-1}) = 372.93 cm^{-1}, has a frequency in the same range.

For the PMCA structure (see Table 1), there are two combination tones: $\widetilde{\omega}_{10}$ (278.85 cm^{-1})$+\widetilde{\omega}_{11}$ (87.21 cm^{-1}) = 366.06 cm^{-1} (each B_2-symmetry) and $\widetilde{\omega}_{12}$ (277.85 cm^{-1})$+\widetilde{\omega}_{13}$ (86.29 cm^{-1}) = 364.14 cm^{-1} (each E-symmetry), which lie above the fundamental band at $\widetilde{\omega}_f = 334.42$ cm^{-1}. Therefore, these tones are expected to shift down in frequency due to their interaction. Additionally, there is an overtone of E-symmetry vibration, $\widetilde{\omega}_{14}$ (164.81 cm^{-1}), located close to but slightly lower than, $\widetilde{\omega}_f = 334.42$ cm^{-1}, which will shift the fundamental vibration to a higher frequency. As a result, the additional structure arising from the FR is expected to appear slightly below $\omega_1 = 338$ cm^{-1}. However, no such bands were observed in the experimental spectrum[20], likely due to their very low intensity. This suggests that the concentration of the PMCA structure in the CZTS crystal is minimal. In the present study, the features observed in the experimental spectrum are analyzed using a

theoretical relation (*intensity of Raman scattering: a brief overview*) that describes the Raman scattering of light in crystals, accounting for the FR.

Numerical calculations and discussion of the experiment for CZTS thin film

In analyzing anharmonic interactions in crystals, particularly FR, knowledge of the phonon density of states (PDOS) is critical. The PDOS depends on the dispersion of the phonon branch participating in the resonance (see Eq. (4c)). If the dispersion of the phonon branches in two directions k_x, k_y is comparable, the PDOS takes a different form. In the case of E-symmetry, where the x and y directions are identical, the PDOS in the one-harmonic approximation of Eq. (4c) is given by curve 1 in Fig. 2. If the dispersion in one direction of the wave vector, k_x, predominates, the PDOS is described in Ref.[27,30].

The anharmonic parameter of the fourth order is considered to be negative, $A \leq 0$. Therefore, in this case, the PDOS is shifted toward lower frequencies and transformed, as seen in Fig. 2. A sharp maximum at the low-frequency edge of the spectrum is referred to as a bi-phonon[40].

A different situation arises when FR is taken into account. In this case, the character of the spectrum depends on the mismatch between the fundamental and the combination tones[27]. Here, the parameters A^p and Γ affect the spectrum similarly, shifting the PDOS towards lower frequencies. Therefore, we set $A^p = 0$ to isolate the effect of the parameter Γ. As Γ increases, a sharp maximum appears on the low-frequency side of PDOS, and the fundamental band ω_f shifts in the opposite direction. As we have shown in our report for the upper group of curves, when $\delta_c < 0$, both A^p and Γ act in opposite directions[27]. Similar trends are expected to occur for the case presented in Fig. 2 as A^p values are varied.

As an example, we consider the case of weak FR, where the difference between the fundamental and combination tone frequencies is large enough for both bands to be clearly observed. However, when the frequencies of both bands are close, the spectrum becomes more complicated. Namely, this situation is experimentally observed (Fig. 1), where the fundamental band at $\omega_1 \approx 338$ cm^{-1} is located near a combination tone at $\widetilde{\omega}_5 + \widetilde{\omega}_7 \approx 362$ cm^{-1}. The latter is formed by two doubly degenerate E-states; therefore, the PDOS function, in this case, should resemble the one presented by curve 1 in Fig. 2. The results of the theoretical analysis for the CZTS crystal were obtained using Eqs. (1–4) for the region of the fundamental band near $\omega_1 \approx 338$ cm^{-1} and the Raman experimental data are shown in Fig. 3 by curves 2 (FR – 1) and 1, respectively.

As shown in Fig. 3, the key features of the experimental spectrum near the fundamental band at $\omega_1 \approx 338$ cm^{-1} are well captured by the theoretical dependencies. At the high-frequency wing of the theoretical curve, two weak maxima are observed: one at $\omega \approx 364$ cm^{-1}, which coincides with the experimental one, and another at $\omega \approx 350$ cm^{-1}, predicted by the calculations, which will be discussed below.

The theoretical spectrum is very sensitive to the fitting parameters. To show the effect of the adjustment parameters on the character of the spectrum, several theoretical dependencies are depicted in Figs. 4 and 5. It can be seen from Fig. 4 that an increasing mismatch, δ_c between the fundamental band and the combination tone strongly alters the wings of the fundamental spectrum. At a sufficiently large value of δ_c, (curve 4), two weakly coupled bands, similar to those in Fig. 2, can be observed. A somewhat different situation is observed in Fig. 5. As the parameter Γ grows, both the shape of the PDOS changes and the distance between the fundamental band and the center of the PDOS distribution increases. The strong transformation of this part of the spectrum is evident in curves 3 and 4.

The parameter β, which characterizes the optical anharmonicity, and also has a noticeable influence on the intensity of the spectrum in the combination tone region. Therefore, variations in the FR conditions and the parameters of the theoretical spectrum allow for the accurate determination of these parameters when describing the experimental spectrum (see SI, Table S4). Similarly, the band at $\omega_2 = 287$ cm^{-1} can also be described. In "Kesterite (KS)" section it was noted that in the region of this band, FR occurs between the fundamental vibration

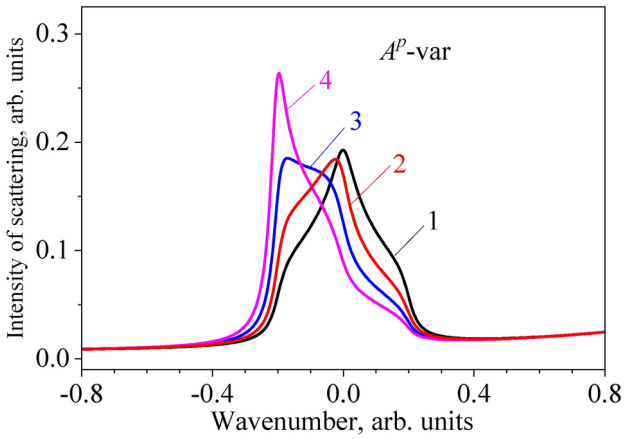

Fig. 2. Intensity of light scattering in the frequency region of two-phonon states at different anharmonic parameters $A^p \leq 0$ (without FR): two-dimensional case $M_1^p = M_2^p \gg M_3^p$, $(\gamma_p = 0.03)$; curve 1, $A^p = -0.001$; curve 2, $A^p = -0.005$; curve 3, $A^p = -0.01$; curve 4, $A^p = -0.015$. (All energy parameters are given in arbitrary units, i.e. $A^p \equiv A^p/M, \Gamma \equiv \Gamma/M$, etc., where $M = 100$ cm^{-1} is a scale factor).

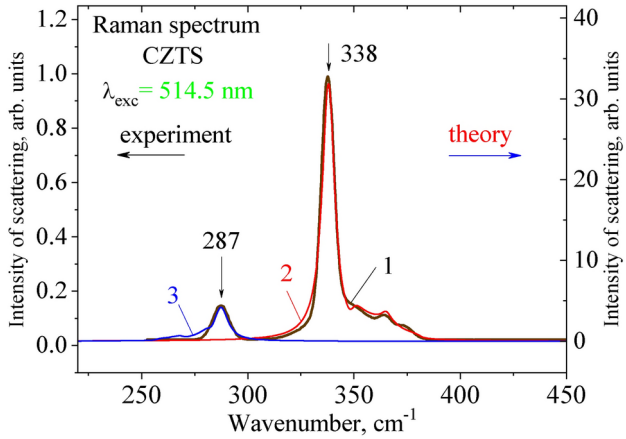

Fig. 3. Comparison of experimental (left, normalized *y*-scale) and theoretical (rights, scale) dependencies obtained for the CZTS film. Curve 1 represents the experimental; curves 2 (FR − 1) and 3 (FR − 2) are theoretical, obtained by accounting for the FR interaction of the fundamental band with a combination tone. The parameters used for these theoretical curves are provided in Table S4.

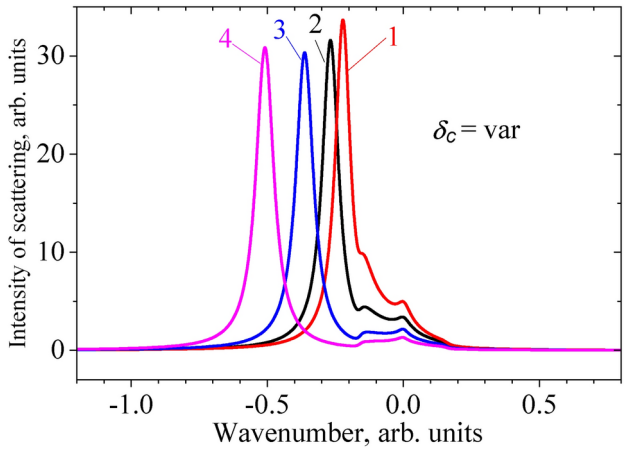

Fig. 4. Influence of the parameter δ_c on the Raman spectrum: curve 1, $\delta_c = 0.2$; curve 2, $\delta_c = 0.25$ (coincides with curve 2 in Fig. 3, obtained by fitting the experimental data); curve 3, $\delta_c = 0.35$; curve 4, $\delta_c = 0.5$.

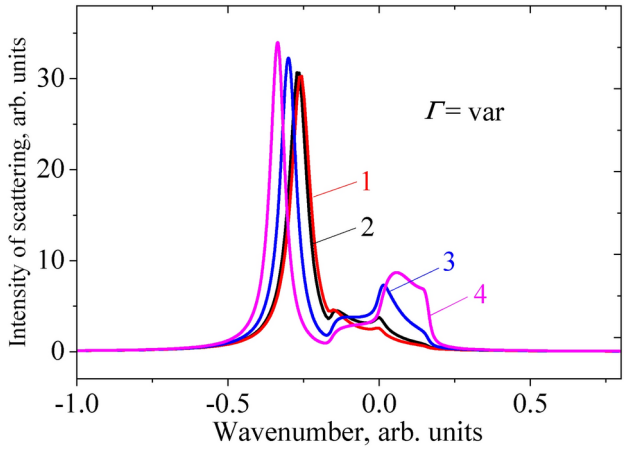

Fig. 5. Influence of the parameter Γ on the Raman spectrum: curve 1, $\Gamma = 0.02$; curve 2, $\Gamma = 0.028$; (which coincides with curve 2 in Fig. 3); curve 3, $\Gamma = 0.05$; curve 4, $\Gamma = 0.07$.

at $\widetilde{\omega}_2 = 284.30$ cm^{-1} (Table 1) and the difference between the two vibration frequencies of B-symmetry: $\widetilde{\omega}_3$ (355.8 cm^{-1})$-\widetilde{\omega}_4$ (86.7 cm^{-1})$=$269.1 cm^{-1}.

The results of the corresponding calculations are presented in Fig. 3, curve 3 (blue). In the range of 260–280 cm^{-1}, in addition to the fundamental band at 287 cm^{-1}, a very weak broadband feature related to the combination tone is observed, which is in good agreement with the experiment (Fig. 1b). The parameters used to fit this fundamental band are shown in Table S4 (FR–2).

Thus, in the present work, we provide a theoretical description of two fundamental bands and their wings for the A and A_1-symmetries. We would like to note that, in the analysis of the strong band at $\omega_1 = 338$ cm^{-1} in Ref.[20], it was emphasized that the correct description of this band is obtained by assuming it consists of two closely spaced frequency peaks, originating from the KS ($\omega_1 = 338$ cm^{-1}) and disordered KS phase, similar to the ST ($\omega_1 = 332$ cm^{-1}) phases (see the legend in Fig. 1b). From our analysis, it follows that the ST structure contributes to the $\omega_1 = 338$ cm^{-1} band. Indeed, the degenerate E states forming the combination tone $\widetilde{\omega}_5 + \widetilde{\omega}_7 \approx 362$ cm^{-1}, which are associated with the ST structure (Table 1), can anharmonically interact with the fundamental vibration at $\omega_1 = 338$ cm^{-1}, which also belongs to the ST structure. Meanwhile, the fundamental band at $\omega_2 = 287$ cm^{-1}, which is related to the KS structure, was discussed in "Kesterite (KS)" section.

Furthermore, according to Table 1, there are several fundamental bands and combination tones of $A(A_1)$-symmetry in the CZTS crystal were not observed experimentally due to their weak intensity. To address this, we conducted a series of targeted experiments using different excitation wavelengths to achieve Raman resonance conditions in specific frequency regions, allowing us to observe the weak-intensity bands more clearly in the polycrystalline thin films under investigation.

First, CZTS Raman spectra measured with different excitation wavelengths were reported in Ref.[54] and further complemented in Ref.[55]. In this report, we analyze and identify Raman-active modes in polycrystalline CZTS thin films using six different excitation wavelengths (325, 457.9, 514.5, 532, 671, and 785.0 nm). In principle, near-resonance Raman effects are expected to be the primary factor influencing changes in the Raman spectra of CZTS with varying excitation wavelengths. Tuning the incident laser wavelength to resonate with a strong electronic interband transition enhances the Raman cross-section, leading to an increase in intensity for vibrational modes associated with that specific transition.

According to the theoretical calculations for the electronic band structure of kesterite performed in Ref.[56], the estimated transition energy for CZTS at the Γ_1 point (the band gap energy) is 1.47 eV, while the transition energy at the Γ_2 point is around 3.50 eV. Considering the energy values for Γ_1 and Γ_2 points, the excitation wavelengths of 785.0, 671, and 325.0 nm, with the corresponding energies of 1.58, 1.85, and 3.81 eV, can be considered optimal for near-resonance Raman scattering effects.

The results of our study are shown in Fig. 6, where the spectra exhibit significant changes with the excitation wavelength λ. All spectra were recorded in the (XX) geometry but they differ significantly depending on the excitation frequency. For all excitation energies, two bands at $\omega_2 = 287$ cm^{-1} and $\omega_1 = 338$ cm^{-1} dominate. The slight shifts in the band positions and their varying broadening were found to depend on the equipment parameters used for the measurements, as noted in the Experimental section. In particular, the spectrophotometer with a grating of 1800 g/mm used for measurement with the 514.5 nm wavelength provided a higher spectral resolution than the other spectrophotometers and wavelengths. The spectrum obtained at λ = 514.5 nm in our work closely resembles the one presented in Ref.[20], where additional structures are reported slightly below ω_2 and slightly above ω_1. However, the Raman spectrum obtained under excitation with λ = 325 nm (violet curve, $h\upsilon_{ex} = 3.82$ eV, close to the resonance at the Γ_2 point ($E_g \approx 3.50$ eV)) demonstrates a significant increase in the peak at $\omega = 346.5$ cm^{-1}. This peak, as predicted in the theoretical analysis of the strong band ω_1 (Fig. 3, curve 2), should be located at ~ 350 cm^{-1} due to the combination tone. On the other hand, Raman spectroscopy is highly sensitive to detecting even trace amounts of ZnS in a sample due to the quasi-resonant excitation of ZnS vibrational modes under these excitation conditions. The spectrum obtained from the CZTS film using UV excitation is dominated by two intense bands at 346 cm^{-1} and 692 cm^{-1}, which are identified as the first- and

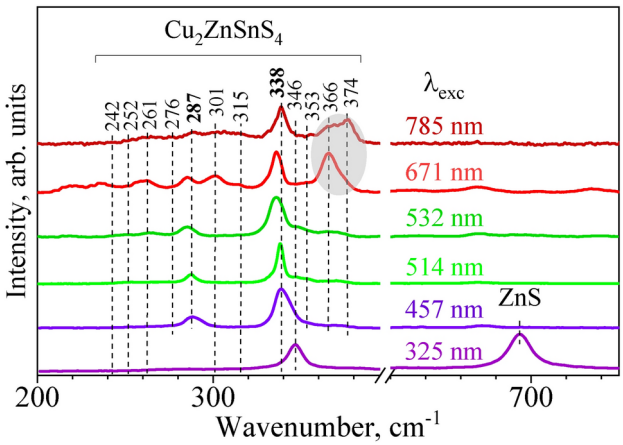

Fig. 6. Raman spectra of polycrystalline CZTS thin film measured at different excitation wavelengths.

second-order longitudinal optical (LO) modes characteristic of the ZnS phase[57]. Notably, the FR enhancement of this combination tone by the fundamental $\omega_1 = 338$ cm^{-1} is significant, and the intensity at the maximum near 350 cm^{-1} in curve 2 is comparable to the intensity at the maximum of the fundamental band at $\omega_2 = 287$ cm^{-1}.

The situation with the band below the fundamental vibration at $\omega_2 = 287$ cm^{-1} is also complex. Upon excitation with $\lambda = 514.5$ nm (light green line in Fig. 6), a broad, flat, and weak band is observed in the range of approximately ~ 250–280 cm^{-1}. However, Ref.[55] shows that under excitation with $\lambda = 325$ nm ($hv_{ex} = 3.82$ eV), this flat band transforms into a structure consisting of three distinct bands. In the theoretical analysis, we suggest that this could be attributed to the FR of the fundamental band at $\omega_2 = 287$ cm^{-1} with the combination tone of A-symmetry (Table 1): 355.80 cm^{-1} – 86.70 cm^{-1} = 269.1 cm^{-1}. Moreover, within this frequency range, there is another combination tone (166.65 cm^{-1} + 98.82 cm^{-1} = 265.47 cm^{-1}) of the same symmetry, resulting in a more complex case of FR involving two combination tones. Since both combination tones share the same symmetry and originate from the same KS crystal structure, they are expected to interact with each other. This type of interaction is known as Darling-Dennisson (DD) resonance, first studied in the H_2O molecule (Ref.[58]). Such interaction causes the two combination tones to repel each other, leading to a band structure with several maxima. In addition, this frequency range includes a peak corresponding to the fundamental band of the KS structure at $\widetilde{\omega} = 272.82$ cm^{-1}, as well as several bands associated with the ST structure: the fundamental at $\widetilde{\omega} = 277.12$ cm^{-1}, and combination tones such as 161.68 cm^{-1} (E) + 97.34 cm^{-1} (E) = 259.02 cm^{-1} and 149.69 cm^{-1} (B_2) + 95.85 cm^{-1} (B_2) = 245.54 cm^{-1}, (see Table 1). All the noted ST bands have A_1-symmetry, according to group theory. Therefore, the broad, flat band observed at $\lambda = 514.5$ nm likely exhibits a complex structure. Resonant excitation at the wavelengths used in our work and in Ref.[54,55], specifically $\lambda = 671$ nm and 785 nm, clearly demonstrates the emergence of this complex structure in the analyzed range. For these excitation wavelengths, a maximum is observed around 261 cm^{-1}, with a shoulder at approximately 242 cm^{-1}, which can be attributed to the DD resonance between the two latter combination tones of A_1-symmetry.

The significant spectrum changes in the region between 290 and 380 cm^{-1} are attributed to the quasi-resonance excitation condition, as the corresponding energies are close to E_g at the Γ_1-point. The peak at 301 cm^{-1} corresponds to the overtone 2 × 149.69 cm^{-1} (B_2), while the peak at 315 cm^{-1} can be assigned to an overtone 2 × 161.68 cm^{-1} and a shift toward lower frequencies due to the FR with the fundamental 338 cm^{-1} band. It should be noted that an increase in excitation power can influence the kesterite spectrum. The shift of the main kesterite band under resonance excitation (785 nm) is associated with the reversible, optically induced phase transformations caused by high excitation power and heating Ref.[48,49,59]. A peak at 366 cm^{-1} is observed in the theoretical dependence (Fig. 3, curve 2). The peak at 374 cm^{-1} can be related to a combination tone (277.08 cm^{-1} (B_2) + 95.85 cm^{-1} (B_2) = 372.93 cm^{-1} (A_1), with a slight shift towards higher frequencies due to the FR with the fundamental band at $\omega_1 = 338$ cm^{-1}. Since this fundamental band participates in the FR interactions with combination tones placed above and below, its middle position remains unchanged as a result of these interactions. The weak bands observed in Ref.[55] at 164 cm^{-1} and 140 cm^{-1} can be assigned to an overtone (2 × 78.39 cm^{-1} (E)) and a combination tone (235.41 cm^{-1} (E) – 97.34 cm^{-1} (E) = 138.07 cm^{-1} (A_1)), respectively. Other low-frequency bands reported in Ref.[55] at 97, 82, and 68 cm^{-1} may correspond either to fundamental vibrations of E or B, B_1, B_2 symmetry observed due to crystal imperfection, or to differences between some fundamental frequencies. Further studies, particularly using different RS geometries, may help clarify the nature of these weak bands.

To summarize, based on the symmetry analysis of phonon bands[20,25,26] and the experimental Raman scattering study, it can be concluded that the actual CZTS structure evidently comprises a combination of two phases: KS and disordered KS phase (similar to ST), which exhibit very similar crystal parameters. Even polarization measurements[60,61] do not clarify the real structure. However, by utilizing the properties of crystal symmetry and multi-wavelength Raman excitation, a clearer understanding of the true features of the CZTS phonon spectra can be achieved.

CZTSe polycrystalline thin film

This thin film can also be crystallized in three structures: KS, ST, and PMCA. The harmonic frequencies for each structure, alongside our DFT calculations, are reported in Refs[20,26]. Some of these frequencies, relevant to the following analysis, are presented in Table 2 of the present work. The calculated frequencies notably differ from the maxima of A-symmetry bands observed in the experimental spectrum[19,20], as shown in Fig. 7: $\omega_1 = 194$ cm^{-1}, $\omega_2 = 171$ cm^{-1}, and a relatively broad, weak band with a maximum at $\omega_3 \approx 232$ cm^{-1}. The Lorentzian deconvolution of the experimental spectrum of the CZTSe polycrystalline thin film is shown in Fig. 7. As with CZTS, in CZTSe, a weaker band at 191 cm^{-1} appears near the most intense band at 194 cm^{-1}. The fitting for the band at 171 cm^{-1} also revealed a feature near 167 cm^{-1}, which was not considered. The degree of disordering in the CZTSe structure was estimated similarly to CZTS, using a ratio of $I_{191}/I_{194} = 0.295$. This ratio is higher than for CZTS, which can be attributed to deviation from stoichiometric composition (deviations from the nominal ratio of 2:1:1:4) in the CZTSe film. This is consistent with the presence of disorders (antisite and point defects) in the kesterite phase, as observed in EDX measurements (Fig. S1j). Additionally, an increase in Zn content relative to stoichiometric Cu content is accompanied by low-frequency shifts of the main A modes (171 and 194 cm^{-1}) compared to the stoichiometric case (~ 2–3 cm^{-1} in our study)[17]. The Zn_{Cu} defect influences the full width at half maximum (FWHM) of the band at 194 cm^{-1}. The FWHM of this band is particularly sensitive to the band at 191 cm^{-1}. Despite these complexities, modeling using Eq. (1) was successfully applied. Therefore, we analyzed each of the three structures (KS, ST, and PMCA) in a manner similar to the analysis of CZTS in the preceding section.

Kesterite				Stannite				PMCA			Experiment
Symmetry	Work[20]	Work[26]	This work	Symmetry	Work[20]	Work[26]	This work	Symmetry	Work[20]	This work	CZTSe
A	213.05	196.2	217.9	A_1	213.83	194.5	187.2	A_1	208.85	192.6	232
	193.01	183.6	179.2		184.50	180.0	179.0		185.44	181.8	194
	188.10	181.0	174.3								
				A_2	–			A_2	–		
B(TO)	93.33	85.4	106.8	B_1				B_1	171.64	177.2	
	85.42	74.4	81.9	B_2				B_2	81.31	80.1	
E_1(TO)				E	155.35	163.1	158.6	E	158.1	149.5	
E_2(TO)	–				100.41	86.2	90.2		85.32	77.2	
					80.77	56.9	71.1		60.03	58.0	

Table 2. The calculated Γ-point phonon frequencies (in cm^{-1}) for the KS, ST, and PMCA structures of CZTSe in this work, along with those reported in Refs.[20,26], are compared with the experimental Raman frequencies of the polycrystalline thin films presented in this study.

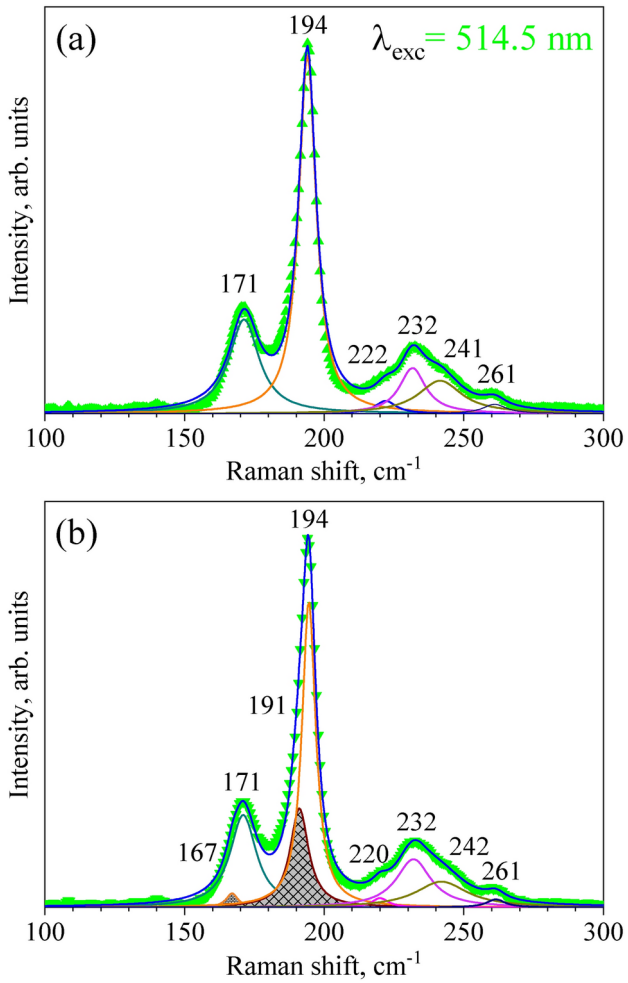

Fig. 7. Raman spectrum of a CZTSe thin film at $\lambda_{ext} = 514.5$ nm (~2.41 eV) and at room temperature is shown. The green line (connecting triangles) represents the sum of the peaks (blue) used to deconvolute the experimental spectrum. (**a**) The most intense RS peaks at $\omega_1 = 194$ cm^{-1} is assumed[20] to originate solely from KS of CZTSe; (**b**) The same peak is assumed[20] to consist of two closely placed peaks: one from KS ($\omega_1 = 194$ cm^{-1}) and the other from disordered KS, similar to the ST phases ($\omega_1 = 191$ cm^{-1}).

Kesterite (KS)

The calculations for the CZTSe KS structure are provided in Table 2, where several A-symmetry frequencies are listed. One of these, $\widetilde{\omega}_4 = 193.01$ cm^{-1} is very close to the overtone $2\widetilde{\omega}_5 = 186.66$ cm^{-1}. Due to FR, both components of the Fermi doublet (the main vibration and the overtone) will shift in opposite directions, and the fundamental band at $\widetilde{\omega}_4 = 193.01$ cm^{-1} will shift to the high-frequency side.

Therefore, the band at $\omega_1 = 194$ cm^{-1} in the experimental spectrum might be considered as originating from the fundamental $\widetilde{\omega}_4$ due to FR. However, the band $\omega_3 \approx 232$ cm^{-1}, also observed in the same A-symmetry, exhibits a distinct form characteristic of E vibrations (see the theoretically calculated spectra in Fig. 2, curve 3). It can therefore only be associated with the combination tone $\widetilde{\omega}_6(155.35\ \text{cm}^{-1}) + \widetilde{\omega}_7(80.77\ \text{cm}^{-1}) = 236.12$ cm^{-1}. Thus, the three experimentally observed bands (171, 194, and 232 cm^{-1}) shown in Fig. 7 are associated with the KS crystal structure. As for the components $\widetilde{\omega}_3 = 193.01$ cm^{-1} and $2\widetilde{\omega}_5 = 186.66$ cm^{-1}, they likely possess too small an intensity to be observed as the band at $\omega_2 = 287$ cm^{-1} in Fig. 1 for the KS structure of CZTS. These components are located between two stronger bands $\omega_1 = 194$ cm^{-1} and $\omega_2 = 171$ cm^{-1}, making them difficult to detect.

Stannite (ST) and PMCA

As noted above, the combination tone (or overtone) of a double degenerate E-state can be observed in A_1 -symmetry. Moreover, it can interact with the fundamental vibration in A_1 symmetry and should be enhanced if the energy gap between them is small. For the ST structure, as indicated in Table 2**,** the following pair of closely spaced bands can be observed: the fundamental $\widetilde{\omega}_8 = 184.50$ cm^{-1}, and the combination tone $\widetilde{\omega}_9(100.41\ \text{cm}^{-1}) + \widetilde{\omega}_7(80.77\ \text{cm}^{-1}) = 181.18$ cm^{-1}. Therefore, both bands should shift even with small anharmonic interactions. As a result of the FR interaction, the fundamental band will shift to the high-frequency region, while the combination tone will shift to the low-frequency region and be enhanced due to resonance. As the fundamental frequency approaches ~ 200 cm^{-1} due to FR interactions, it begins to interact more strongly with the combination tone $\widetilde{\omega}_6 + \widetilde{\omega}_7 = 236.12$ cm^{-1}, which also enhances it. However, this effect will be weak due to the significant frequency gap between the two combination tones. Thus, each FR interaction should be considered individually. It should be noted that in the region of the combination tone for the ST structure, $\widetilde{\omega}_6 + \widetilde{\omega}_7 = 236.12$ cm^{-1}, a similar combination tone is also observed in the PMCA structure: $\widetilde{\omega}_{10}(158.10\ \text{cm}^{-1}) + \widetilde{\omega}_{11}(85.32\ \text{cm}^{-1}) = 243.42$ cm^{-1} (Table 2). However, since this structure is not close to the fundamental, the corresponding combination tone is expected to be weak. For this reason, we will focus on the features related to the ST structure.

Simulation and discussion of experimental spectra of CZTSe film

As noted above, the principal influence on the position of the calculated bands and their intensity can generally be attributed to anharmonic effects in the ST structure of the CZTSe film. The Raman spectrum and the fitted theoretical dependence for CZTSe are shown in Fig. 8. The theoretical curve 2 (FR-3) describes the strong FR between the closely located fundamental band $\widetilde{\omega}_8 = 184.50$ cm^{-1} and a combination tone $\widetilde{\omega}_9(100.41\ \text{cm}^{-1}) + \widetilde{\omega}_7(80.77\ \text{cm}^{-1}) = 181.18$ cm^{-1}. It increases significantly due to FR and reaches an intensity comparable to that of the fundamental band. Another combination tone, $\widetilde{\omega}_6 + \widetilde{\omega}_7 = 236.12$ cm^{-1} participates in weak FR with the new fundamental band $\widetilde{\omega}_8^{new} \approx 198$ cm^{-1} (curve 3, FR-4), as it is sufficiently separated from the latter.

It is noteworthy that in the region around ~ 215–225 cm^{-1}, there is a lack of good correlation between the experiment and the theory. Ref.[16] demonstrates how the ratio of components (the deviation from the nominal ratio of 2:1:1:4 in kesterite) affects the structural and optical properties, including the Raman spectra. A more detailed analysis of the impact of compositionally induced defects on the vibrational properties of CZTSe absorbers is presented in Ref.[17]. In our case, an increase in Zn content and a decrease in Sn content in the CZTSe

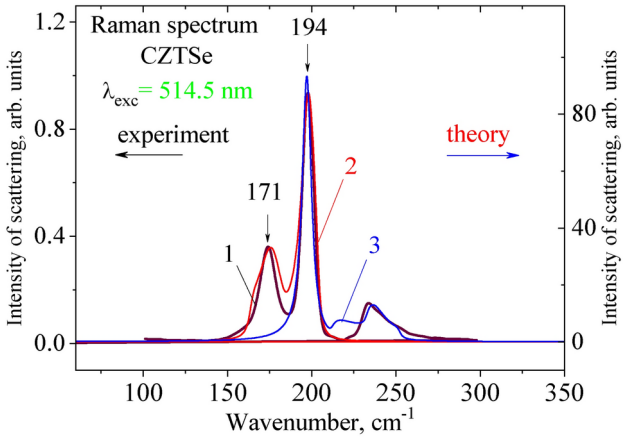

Fig. 8. Comparison of the theoretical dependencies for CZTSe with experimental data. Curve 1 represents the experimental; curves 2 (FR-3) and 3 (FR-4) are theoretical, and obtained by considering the FR interaction between the fundamentals and combination tones (the parameters used for these calculations are given in Table S4).

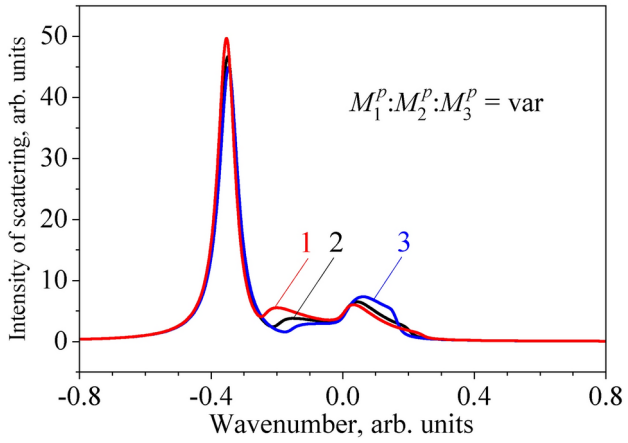

Fig. 9. The change in the spectrum in the region of two-phonon excitations as a function of the dispersion of the phonon branch is shown for the following cases: curve 1, $M_1^p = 0.06$, $M_2^p = 0.06$, $M_3^p = 0.005$; curve 2, $M_1^p = 0.05$, $M_2^p = 0.05$, $M_3^p = 0.005$; curve 3, $M_1^p = 0.04$, $M_2^p = 0.04$, $M_3^p = 0.005$.

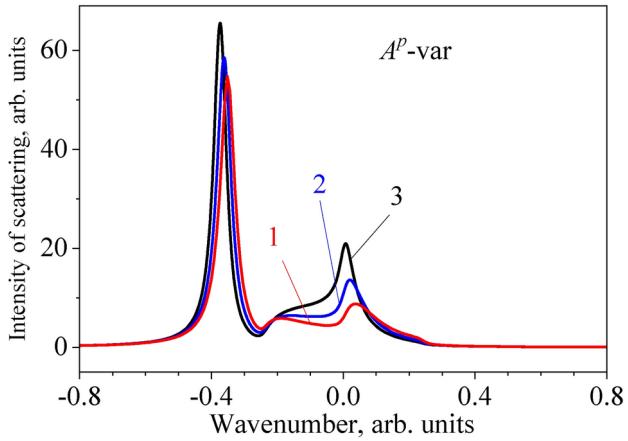

Fig. 10. Influence of the anharmonic parameter A^p on the Raman spectrum in the presence of FR interaction: curve 1, $A^p = 0.005$; curve 2, $A^p = 0.01$; curve 3, $A^p = 0.015$.

film contribute to the appearance of a Zn_{Sn} defect (Fig. S1j). Thus, the deviation from nominal stoichiometry leads to a higher intensity in the ~ 215–225 cm^{-1} frequency range. This discrepancy may also be related to a lack of knowledge regarding the phonon branch dispersion involved in FR. The effect of dispersion is clearly evident in Fig. 9, where the maximum observed between the fundamental mode and the combination tone becomes smaller with the decreasing of parameters M_j^p. Simultaneously, the shape of the peaks in the two-phonon excitation region (as shown in Fig. 9) also changes. From Table 2, it can be seen that the combination tone $\widetilde{\omega}_6$ (155.35 cm^{-1}) + $\widetilde{\omega}_9$(100.41 cm^{-1}) = 255.76 cm^{-1} is positioned immediately after the band with a maximum of around 232 cm^{-1}, which makes this band broader and more extends it into the high-frequency region. Based on reference data and our results, it can be concluded that the deviation from stoichiometry in the films did not cause the appearance of new bands. However, the broadening, accompanied by a slight shift in bands, does not reduce the quality of the given computations but rather demonstrates their effectiveness even in a more complex case.

In Fig. 10, it can be seen that the anharmonic parameter A^p has a notable influence on the spectrum of two-phonon excitations in the absence of FR[27]. However, when FR occurs, both anharmonic parameters Γ and A^p affect the spectrum, depending on the ratio of these parameters and the sign of the δ_c the parameter, (i.e.,$\delta_c > 0, \delta_c < 0$)[27]. As an example, Fig. 10 illustrates the case of $\delta_c < 0 (\omega_0^f < \omega_0^\mu + \omega_0^\upsilon)$. Here, the constant Γ causes state repulsion, resulting in a maximum appears on the right-hand side of the spectrum. Meanwhile, A^p shifts the entire spectrum to the low-frequency side and compresses it, as shown by curve 4 in Fig. 2.

The change in the relative intensities of the fundamental band and an overtone can be tuned by fitting the parameter β, as shown in Fig. 11. Therefore, the effect of all anharmonic constants is crucial for analyzing and understanding the experimental spectrum. For the studied crystals, it can be concluded that the general features of the experimental spectrum are well captured by the theoretical approach presented in Section *Intensity of Raman scattering: a brief Overview*, Eqs. (1–4). It is evident that the strongest effect on the spectrum comes

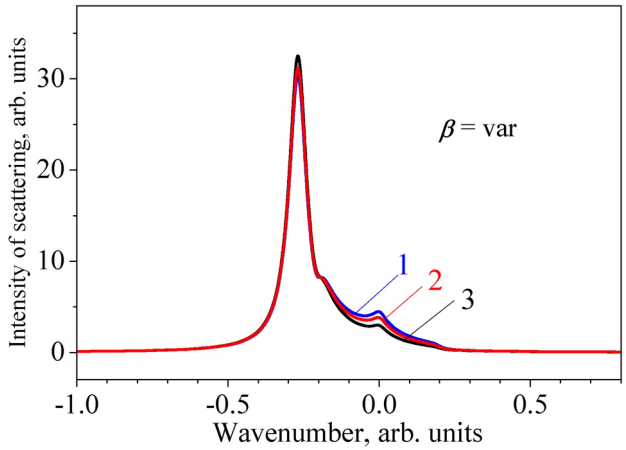

Fig. 11. Influence of the parameter β on the Raman spectra: curve 1, $\beta = 0.1$; curve 2, $\beta = 0.08$; curve 3, $\beta = 0.05$.

from the Γ and δ_c parameters, particularly in the combination tone frequency region. By fitting the model spectra to the experimental Raman data, we can estimate the specific value of these parameters. In particular, this allows for the estimation of the anharmonic parameters Γ, β and A^p, which are listed in Table S4. The fitting result reveals that the cubic term (Γ) contributes significantly to the frequency shift for both CZTS and CZTSe materials, compared to the relatively small contribution from the fourth-order term (A^p), as shown in Ref.[29]. Table S4 supports the assertion that anharmonic interactions exhibit similar magnitudes in the kesterite and stannite structures of CZTS and CZTSe. This finding indicates a relatively weak level of anharmonicity in these structures, as also demonstrated in Ref.[62]. Additionally, the values of the $M^v_{l,j}$ parameters, which characterize the width of phonon dispersion[27,31], can also be estimated. It is worth noting that while these parameters can also be derived from DFT calculation, obtaining them is not a straightforward task.

One should note that anharmonism must be considered an important factor in nanocrystals, as it can significantly impact their electronic, optical, and thermal properties. As is well known, when the size of the crystal decreases, the surface area-to-volume ratio increases, resulting in a higher density of surface defects and intensified surface vibrations. Many intriguing features can be observed in nanocrystals; for instance, an abnormal positive shift of Raman bands, which contrasts with the traditional negative shift commonly observed in nanocrystals as their size decreases[62]. Thus, we believe that our current theoretical approach, based on anharmonic effects and the formalism developed in our previous studies[27,30,63], could offer insights into understanding and explaining the features observed in Refs.[28,29]. Moreover, this theoretical approach will be particularly relevant for analyzing anharmonism in nanocrystals, where the impact of these effects is expected to be substantial. However, all these intriguing matters will be addressed in our forthcoming research. Therefore, further theoretical and experimental studies in this area may lead to new strategies for optimizing the optical and electronic properties of CZTS and help unlock its full potential as a low-cost and sustainable alternative to conventional photovoltaic materials.

Methods

Sample preparation and characterization

The CZTS and CZTSe polycrystalline thin films were deposited using two-step and one-step processes. More detailed information about the samples can be found in our previous works[64–66] and in the Supplementary Information (SI), Fig. S1. The surface morphology and the composition elements mapping of the thin films were analyzed using a scanning electron microscope (SEM) and energy dispersive X-ray (EDX) (Zeiss Instruments INCA X-Sight) combined with a Zeiss Sigma 500 SEM. The morphology, cross-sections, and EDX measurements were performed at a 15 kV operating voltage. The thicknesses of all the studied semiconductor layers and that of the Mo layer were evaluated to be approximately ~1 μm (Fig. S1). Structural characterization was carried out at room temperature using X-ray diffraction (XRD) and Raman spectroscopy[67–69]. XRD measurements were performed in the Bragg Brentano configuration, using a PANalytical X'pert Pro MPD diffractometer with Cu-Kα-radiation (λ = 1.54056 Å)[70]. Reflection and transmittance spectra were recorded using a Shimadzu UV-3600 spectrometer[71].

For Raman spectroscopy, Horiba LabRAM HR Evolution and WITec Alpha300Ri spectrometers were employed in the backscattering configuration. The HR Evolution system used an Ar^+ ion laser (514.5 nm) and HeCd lasers (325.0 nm) for excitation, with an Olympus microscope facilitating both excitation and light collection. The laser spot size was approximately 2 μm, depending on the wavelength. The WITec Alpha300R spectrometer used a diode laser with 785 nm excitation and an inverted Olympus microscope with a similar laser spot size. The MDR 23 monochromator (LOMO) with a cooled Andor CCD detector (Oxford Instruments, UK) operated with a triple diode lasers system (Nd: YAG Diode-Pumped Solid-State-DPSS), utilizing 457.9 nm, 532 nm, and 671 nm excitation lines, with a 100 μm spot size on the sample[72–76]. The excitation density was kept below 10^5 W/cm^2 to prevent thermal effects in the spectra. Before and after acquiring each Raman spectrum, the

first-order Raman spectrum of monocrystalline Si was measured as a reference, and the spectra were corrected based on the Si line at 520 cm^{-1}[77–80]. Additionally, the Raman equipment and software included a protocol to calculate the observed and instrumental profiles to obtain the actual profile. Therefore, we did not calculate this equipment parameter directly. All measurements were conducted at room temperature in the same areas of the films to avoid the influence of different component ratio distributions, as shown in the SI.

Lattice dynamics calculations and intensity of Raman scattering: a brief overview

First-principles calculations were performed using the Perdew-Burke-Ernzerhof (PBE) functional[81], a specific formulation of the Generalized Gradient Approximation (GGA) for the exchange–correlation (XC) term, along with ultrasoft Vanderbilt pseudopotentials to model the interactions between electrons and ions. A plane-wave basis set was used for wavefunction expansion, with a kinetic energy cutoff set at 60 Ry/atom. The Brillouin zone was sampled using a Monkhorst–Pack *k*-point grid with dimensions 6×6×6, centered at the Γ-point[82]. To optimize different crystalline structures of CZT(S,Se), full relaxation was performed, ensuring that residual forces were below a threshold of 10^{-5}Ry/a.u. To compute phonon frequencies at the Γ- point of the Brillouin zone, density functional perturbation theory (DFPT), as implemented in the phonon code of the Quantum Expresso software, was used[83].

The modeling of Raman spectra in the presence of anharmonic interactions was performed using the theoretical approach developed in Refs.[27,30,40]. The relations describing the spectral dependence of Raman scattering (RS) intensity in the case of the FR are similar to those presented in Ref.[32]. Anharmonic parameters $\widetilde{\beta}$, and $\widetilde{\Gamma}$,$\widetilde{A}^p$, that characterize optical and mechanical anharmonicity, respectively, as well as components of light scattering tensors χ_{pp}, χ_c, and frequencies $\widetilde{\omega}_{Q,p}, \widetilde{\omega}_{Q,c}$, depend on the temperature in the present consideration (this is denoted by an index "~"). All simulated spectra were modeled for room temperature. The temperature effect can be significant if the temperature varies over a wide range of values: $T_1 > T_{room} > T_2$. The equations describing the RS intensity are as follows (see Eq. (12) in Ref.[30,32]):

$$I(\omega) \sim [1 + n(\omega)] \widetilde{\chi}_c^2 \frac{2f_2a^2 + R_2^c b^2}{c^2 + d^2}, \tag{1}$$

where

$$a^2 = \left(\widetilde{\Gamma} + \widetilde{\beta}\Delta^c\right)^2 + \left(\widetilde{\beta}R_2^c\right)^2, \tag{2a}$$

$$b^2 = \left[1 + 2f_1(\widetilde{A}^p + \widetilde{\beta}\widetilde{\Gamma})\right]^2 + \left[2f_2(\widetilde{A}^p + \widetilde{\beta}\widetilde{\Gamma})\right]^2, \tag{2b}$$

$$c = \Delta^c + 2f_1\left(\widetilde{A}^p\Delta^c - \widetilde{\Gamma}^2\right) + 2f_2\widetilde{A}^pR_2^c, \tag{2c}$$

$$d = 2f_2(\widetilde{A}^p\Delta^c - \widetilde{\Gamma}^2) - (1 + 2f_1\widetilde{A}^p)R_2^c, \tag{2d}$$

$$f(\omega) = f_1 + if_2 = \frac{1}{N}\sum_q \frac{1 + 2n_q^p}{\omega - 2\widetilde{\omega}_{q,p} + i\gamma_p}, \tag{3}$$

$$\Delta^c = \omega - \widetilde{\omega}_{Q,c}, \widetilde{\omega}_{Q,c} = \omega_{Q,c} + \sum_s \eta_{s,s}^{c,c}(1 + 2n_s), \widetilde{\omega}_{Q,p} = \omega_{Q,p} + \sum_s \eta_{s,s}^{p,p}(1 + 2n_s), \tag{4a}$$

$$\widetilde{\Gamma} = \Gamma + \sum_s \eta_{s,s}^{c,pp}(1 + 2n_s), \widetilde{A}^p = A^p + \sum_s \eta_{s,s}^{p,p}(1 + 2n_s), \tag{4b}$$

$$\omega_{k,v} = \omega_{0,v} + \sum_{l=1}^{L}\left[M_{l,x}^v\cos(lk_xa_x) + M_{l,y}^v\cos(lk_ya_y) + M_{l,z}^v\cos(lk_za_z)\right], v = p, c. \tag{4c}$$

Here, $f(\omega)$ is a complex function that characterizes the density of two-phonon states (TPS) participating in the FR. The TPS provides insights into the anharmonic interactions between phonons and is an essential factor at the nanoscale, where anharmonicity significantly influences thermal and electronic transport properties. The parameters: $\widetilde{\beta} = \widetilde{\chi}_{pp}/\widetilde{\chi}_c$; $\widetilde{\chi}_c, R_2^c$, and $\widetilde{\chi}_{pp}, \gamma_p$ are the scattering tensor per unit cell and the damping constants of the fundamental vibration (subscript *c*) and the overtone (subscript *pp*) respectively. Damping arises due to the interaction between the *c*- and *pp*-vibrations with other lattice vibrations.The dispersion of phonon frequencies, $\omega_{k,v}$ is approximated by a series of harmonics in *k*-space and $M_{l,j}^v$ characterizes the value of dispersion (see more details in Refs.[32,40]). $\eta_{s,s}^{c,c} < 0, \eta_{s,s}^{p,p} < 0$ are fifth-order anharmonic constants. The initial values of phonon frequencies $\omega_{0,v}$ were taken in harmonic approximation from DFT calculation at the *Γ*-point from Ref.[20] (hereafter, DFT-calculated frequencies are denoted with the index "~"). In theoretical calculations, it is convenient to use the parameter $\delta_c = \omega_c - 2\omega_p, where Q \to 0$, which describes the energy difference between the Fermi-interacting states. It is important to note that the proper relation for Raman intensity was obtained for non-resonance cases. To include the resonance effect in the current relation, we would need to add the electron and electron–phonon parts in the Hamiltonian system, as shown in our previous work[84]. Therefore, our study focuses on non-resonance Raman scattering when the electron–phonon coupling is weak (see Ref.[29]). However, our theory can be employed as a useful approximation for studying resonance Raman phenomena in CZTS(Se) materials. Overall, in analyzing experimental results, we can use the harmonic values of phonon frequencies

at the Γ-point obtained from DFT calculations, which are associated with the crystal space groups of the KS, ST, and PMCA structures, as reported in Refs.[20–22,85]. Incorporating anharmonic effects into DFT calculations demands significantly more computational resources and advanced numerical techniques compared to simple harmonic approximations. Therefore, a more practical theoretical approach to studying anharmonic effects in CZTS(Se) crystals is to utilize simplified analytical models, which can effectively and accurately capture their vibrational properties.

Symmetry relations for the combination states

According to group theory, the representation of a combination tone can be calculated using the known relationship between the characters of the corresponding representations as follows:

$$\{\chi_\mu^2(g)\}_\pm = \frac{1}{2}\{\left[\chi_\mu(g^2)\right]^2 \pm \chi_\mu(g^2)\} \tag{5}$$

The number of irreducible representations $\chi_j(g)$ included in $\{\chi_\mu^2(g)\}_\pm = \widetilde{\chi}_\mu(g)$ is calculated using the relation, where for identical representations, the sign "+" should be taken:

$$r_j = \frac{1}{h}\sum_g \widetilde{\chi}^*(g)\chi_j(g) \tag{6}$$

In Eqs. (5) and (6), the following designations are introduced: $\chi_j(g)$ is the j-th irreducible representation, g and h are elements of the point group, with their corresponding orders, respectively.

It was noted in Ref.[20] that the space group symmetries for each crystal structure (see Fig. S2 for KS, ST, and PMCA) are different, and anharmonic interactions leading to the mixing of states should also depend on the symmetry of each structure. Therefore, it is convenient to study the three above-mentioned CZTS (CZTSe) structures separately.

Conclusions

The investigation has shown that anharmonic interactions in CZTS and CZTSe films are significant for understanding the features of their Raman spectra. In addition to numerical calculations of the harmonic phonon frequencies, the actual positions of bands and the redistribution of their intensities caused by anharmonic interactions must be taken into account. We have studied the effects of anharmonic interactions between a fundamental vibration and an overtone (combination tone) in CZTS and CZTSe for three structures: KS, ST, and PMCA, at room temperature and non-resonant excitation. The detailed analysis revealed trends in the variation of the Raman spectra in the films, with key theoretical parameters Γ and A, describing the contributions of third- and fourth-order anharmonicity changes.

For the first time, FR features of crystal structures with different symmetries within the framework of the same theoretical approach, have been described based on experimental Raman results for CZTS(Se). The theoretical analysis shows that the FR phenomenon is more complex in the case of crystals due to the participation of the entire TPS band in the resonance interactions. The spectral features in solids include the fundamental vibration band, overtone, and the TPS band. Additionally, experiments using multi-wavelength excitation enabled us to discover and conduct a detailed analysis of weak bands, which are much more prominent than allowed by the selection rules for some geometries of scattering in the CZT(S,Se) films. Thus, by considering the anharmonic contributions to the phonon spectra, it is possible to obtain a more accurate description of the vibrational properties of different CZT(S,Se) structures, which can have significant implications for understanding their electronic and optical properties. The results can also be useful for optimizing the performance of CZTS-based solar cells by tuning the material's vibrational behavior.

Data availability

The data presented in this study are available on request from the corresponding author.

Received: 7 June 2024; Accepted: 11 December 2024
Published online: 02 January 2025

References

1. Sawa, H. B. et al. Enhanced performance of Cu_2ZnSnS_4 based bifacial solar cells with FTO and W/FTO back contacts through absorber air annealing and Na incorporation. *Sol. Energy Mater. Sol. Cells* **264**, 112605. https://doi.org/10.1016/j.solmat.2023.112605 (2024).
2. Olgar, M. A., Erkan, S. & Zan, R. Dependence of CZTS thin film properties and photovoltaic performance on heating rate and sulfurization time. *J. Alloys Compd.* **963**, 171283. https://doi.org/10.1016/j.jallcom.2023.171283 (2023).
3. Kapush, O. A. et al. Raman study of colloidal Cu_2ZnSnS_4 nanocrystals obtained by "green" synthesis modified by seed nanocrystals or extra cations in the solution. *Heliyon* **9**, e16037. https://doi.org/10.1016/j.heliyon.2023.e16037 (2023).
4. Pakštas, V. et al. Improvement of CZTSSe film quality and superstrate solar cell performance through optimized post-deposition annealing. *Sci. Rep.* **12**, 16170. https://doi.org/10.1038/s41598-022-20670-1 (2022).
5. Solovan, M. N. et al. Structural and optical properties of $Cu_2ZnSn(S, Se_)4$ films obtained by magnetron sputtering of a C_u2ZnSn alloy target. *Phys. Solid State* **59**, 1643–1647. https://doi.org/10.1134/s1063783417080261 (2017).
6. Akcay, N. et al. Cu_2ZnSnS_4 films prepared by a hybrid PVD deposition system: a multi-layered graphitic carbon intermediate layer at the Mo/CZTS interface. *J. Mater. Sci. Mater. Electron.* **35**, 2061. https://doi.org/10.1007/s10854-024-13854-0 (2024).
7. Olekseyuk, I. D. et al. Single crystal preparation and crystal structure of the $Cu_2Zn/Cd, Hg/SnS_e4$ compounds. *J. Alloys Compd.* **340**, 141–145. https://doi.org/10.1016/s0925-8388(02)00006-3 (2002).

8. Zhou, J. et al. Control of the phase evolution of kesterite by tuning of the selenium partial pressure for solar cells with 13.8% certified efficiency. *Nat. Energy* **8**, 526–535. https://doi.org/10.1038/s41560-023-01251-6 (2023).
9. Shi, J. et al. Multinary alloying for facilitated cation exchange and suppressed defect formation in kesterite solar cells with above 14% certified efficiency. *Nat. Energy* https://doi.org/10.1038/s41560-024-01551-5 (2024).
10. Pal, K., Singh, P., Bhaduri, A. & Thapa, K. B. Current challenges and future prospects for a highly efficient (>20%) kesterite CZTS solar cell: A review. *Sol. Energy Mater. Sol. Cells* **196**, 138–156. https://doi.org/10.1016/j.solmat.2019.03.001 (2019).
11. Shockley, W. & Queisser, H. J. Detailed balance limit of efficiency of p-n junction solar cells. *J. Appl. Phys.* **32**, 510–519. https://doi.org/10.1063/1.1736034 (1961).
12. Gokmen, T., Gunawan, O., Todorov, T. K. & Mitzi, D. B. Band tailing and efficiency limitation in kesterite solar cells. *Appl. Phys. Lett.* **103**, 103506. https://doi.org/10.1063/1.4820250 (2013).
13. Li, J. B., Chawla, V. & Clemens, B. M. Investigating the role of grain boundaries in CZTS and CZTSSe thin film solar cells with scanning probe microscopy. *Adv. Mater.* **24**, 720–723. https://doi.org/10.1002/adma.201103470 (2012).
14. Maria, E. & Baten, M. Z. Role of bulk- and interface-defects in spectrum-dependent energy harvesting of CZTSSe-based indoor photovoltaic devices. *AIP Adv.* **11**, 035003. https://doi.org/10.1063/5.0039462 (2021).
15. Mutter, D. & Dunham, S. T. Calculation of defect concentrations and phase stability in Cu_2ZnSnS_4 and $Cu_2ZnSnSe_4$ from stoichiometry. *IEEE J. Photovolt.* **5**, 1188–1196. https://doi.org/10.1109/jphotov.2015.2430015 (2015).
16. Schorr, S. et al. Point defects, compositional fluctuations and secondary phases in non-stoichiometric kesterites. *J. Phys. Energy* **2**, 012002. https://doi.org/10.1088/2515-7655/ab4a25 (2019).
17. Dimitrievska, M., Fairbrother, A., Saucedo, E., Pérez-Rodríguez, A. & Izquierdo-Roca, V. Influence of compositionally induced defects on the vibrational properties of device grade $Cu_2ZnSnSe_4$ absorbers for kesterite based solar cells. *Appl. Phys. Lett.* **106**, 073903. https://doi.org/10.1063/1.4913262 (2015).
18. Dimitrievska, M. et al. Raman scattering analysis of the surface chemistry of kesterites: Impact of post-deposition annealing and Cu/Zn reordering on solar cell performance. *Sol. Energy Mater Sol. Cells.* **157**, 462–467. https://doi.org/10.1016/j.solmat.2016.07.009 (2016).
19. Altosaar, M. et al. $Cu_2Zn_{1-x}Cd_xSn(Se_{1-y}S_y)_4$ solid solutions as absorber materials for solar cells. *Phys. Status Solidi A* **205**, 167–170. https://doi.org/10.1002/pssa.200776839 (2008).
20. Khare, A. et al. Calculation of the lattice dynamics and Raman spectra of copper zinc tin chalcogenides and comparison to experiments. *J. Appl. Phys.* **111**, 083707. https://doi.org/10.1063/1.4704191 (2012).
21. Ramkumar, S. P. et al. First-principles investigation of CZTS Raman spectra. *Phys. Rev. Mater.* **6**, 035403. https://doi.org/10.1103/PhysRevMaterials.6.035403 (2022).
22. Ramkumar, S. P. et al. First-principles investigation of the structural, dynamical, and dielectric properties of kesterite, stannite, and PMCA phases of Cu_2ZnSnS_4. *Phys. Rev. B* **94**, 224302–224310. https://doi.org/10.1103/PhysRevB.94.224302 (2016).
23. Dimitrievska, M. et al. Structural polymorphism in "kesterite" Cu_2ZnSnS_4: Raman spectroscopy and first-principles calculations analysis. *Inorg. Chem.* **56**, 3467–3474. https://doi.org/10.1021/acs.inorgchem.6b03008 (2017).
24. Skelton, J. M., Jackson, A. J., Dimitrievska, M., Wallace, S. K. & Walsh, A. Vibrational spectra and lattice thermal conductivity of kesterite-structured Cu_2ZnSnS_4 and $Cu_2ZnSnSe_4$. *APL Mater.* **3**, 041102–041106. https://doi.org/10.1063/1.4917044 (2015).
25. Khare, A., Himmetoglu, B., Cococcioni, M. & Aydil, E. S. First principles calculation of the electronic properties and lattice dynamics of $Cu_2ZnSn(S_{1-x}Se_x)_4$. *J. Appl. Phys.* **111**, 123704–123708. https://doi.org/10.1063/1.4728232 (2012).
26. Gürel, T., Sevik, C. & Çağın, T. Characterization of vibrational and mechanical properties of quaternary compounds Cu_2ZnSnS_4 and $Cu_2ZnSnSe_4$ in kesterite and stannite structures. *Phys. Rev. B* **84**, 205201–205207. https://doi.org/10.1103/PhysRevB.84.205201 (2011).
27. Nosenko, V. V., Rudko, G. Y., Yaremko, A. M., Yukhymchuk, V. O. & Hreshchuk, O. M. Anharmonicity and Fermi resonance in the vibrational spectra of a CO_2 molecule and CO_2 molecular crystal: similarity and distinctions. *J. Raman Spectrosc.* **49**, 559–568. https://doi.org/10.1002/jrs.5297 (2018).
28. Sarswat, P. K., Free, M. L. & Tiwari, A. Temperature-dependent study of the Raman A mode of Cu_2ZnSnS_4 thin films. *Phys. Status Solidi B* **248**, 2170–2174. https://doi.org/10.1002/pssb.201046477 (2011).
29. Suss, N., Ritscher, A., Lerch, M. & Efthimiopoulos, I. Anharmonic effects in ordered kesterite-type Cu_2ZnSnS_4. *Solids* **2**, 385–394. https://doi.org/10.3390/solids2040024 (2021).
30. Yaremko, A. M. et al. Anharmonic interactions and temperature effects in Raman spectra of Si nanostructures. *Solid State Commun.* **195**, 39–42. https://doi.org/10.1016/j.ssc.2014.06.020 (2014).
31. Valakh, M. Y. et al. Fermi resonance in the phonon spectra of quaternary chalcogenides of the type Cu_2ZnGeS_4. *J. Phys. Condens. Matter.* **28**, 065401. https://doi.org/10.1088/0953-8984/28/6/065401 (2016).
32. Ratajczak, H., Yaremko, A. M. & Baran, J. Fermi resonances in the vibrational spectra of $CsHSeO_4$ crystals. *J. Mol. Struct.* **275**, 235–247. https://doi.org/10.1016/0022-2860(92)80199-r (1992).
33. Fermi, E. Über den Ramaneffekt des Kohlendioxyds. *Zs. f. Phys.* **71**, 250–259. https://doi.org/10.1007/bf01341712 (1931).
34. Yukhymchuk, V. O. et al. Structure and vibrational spectra of $ReSe_2$ nanoplates. *J. Raman Spectrosc.* **51**, 1305–1314. https://doi.org/10.1002/jrs.5898 (2020).
35. Romaniuk, Y. A. et al. Influence of anharmonicity and interlayer interaction on Raman spectra in mono- and few-layer MoS_2: A computational study. *Phys. E: Low-Dimens. Syst. Nanostructures.* **136**, 114999. https://doi.org/10.1016/j.physe.2021.114999 (2022).
36. Yaremko, A. M., Yukhymchuk, V. O., Romanyuk, Y. A., Baran, J. & Placidi, M. Theoretical and experimental study of phonon spectra of bulk and nano-sized MoS_2 layer crystals. *Nanoscale Res. Lett.* **12**, 82. https://doi.org/10.1186/s11671-016-1808-8 (2017).
37. Scott, J. F. Evidence of coupling between one- and two-phonon excitations in quartz. *Phys. Rev. Lett.* **21**, 907–910. https://doi.org/10.1103/PhysRevLett.21.907 (1968).
38. Scott, J. F. Hybrid phonons and anharmonic interactions in $AlPO_4$. *Phys. Rev. Lett.* **24**, 1107–1110. https://doi.org/10.1103/PhysRevLett.24.1107 (1970).
39. Barker, A. S. & Hopfield, J. J. Coupled-optical-phonon-mode theory of the infrared dispersion in $BaTiO_3$, $SrTiO_3$, and $KTaO_3$. *Phys. Rev. A* **135**, A1732–A1737. https://doi.org/10.1103/PhysRev.135.A1732 (1964).
40. Lisitsa, M. P. & Yaremko, A. M. *Resonance Fermi (in Russian)*. 264 (Naukova Dumka, 1984).
41. Fano, U. Effects of configuration interaction on intensities and phase shifts. *Phys. Rev.* **124**, 1866–1878. https://doi.org/10.1103/PhysRev.124.1866 (1961).
42. Reshak, A. H. et al. Structural, electronic and optical properties in earth-abundant photovoltaic absorber of Cu_2ZnSnS_4 and $Cu_2ZnSnSe_4$ from DFT calculations. *Int. J. Electrochem. Sci.* **9**, 955–974 (2014).
43. Tuschel, D. Peak shape and closely spaced peak convolution in Raman spectra. *Spectroscopy* **36**, 10–14. https://doi.org/10.56530/spectroscopy.ba4682f3 (2021).
44. Choudhari, N. J., George, S. D. & Raviprakash, Y. Influence of sulfurization time and Cu-ZnS-Sn stack order on the properties of thermally evaporated CZTS thin films. *J. Mater. Sci. Mater. Electron.* **33**, 5341–5350. https://doi.org/10.1007/s10854-022-07729-5 (2022).
45. Fontané, X. et al. Vibrational properties of stannite and kesterite type compounds: Raman scattering analysis of $Cu_2(Fe, Zn)Sn_S4$. *J. Alloys Compd.* **539**, 190–194. https://doi.org/10.1016/j.jallcom.2012.06.042 (2012).
46. Lafond, A., Choubrac, L., Guillot-Deudon, C., Deniard, P. & Jobic, S. Crystal structures of photovoltaic chalcogenides, an intricate puzzle to solve: the cases of CIGSe and CZTS materials. *Z. Anorg. Allg. Chem.* **638**, 2571–2577. https://doi.org/10.1002/zaac.201200279 (2012).

47. Choubrac, L., Lafond, A., Guillot-Deudon, C., Moëlo, Y. & Jobic, S. Structure flexibility of the Cu_2ZnSnS_4 absorber in low-cost photovoltaic cells: from the stoichiometric to the copper-poor compounds. *Inorg. Chem.* **51**, 3346–3348. https://doi.org/10.1021/ic202569q (2012).
48. Valakh, M. Y. et al. Optically induced structural transformation in disordered kesterite Cu_2ZnSnS_4. *JETP Lett.* **98**, 255–258. https://doi.org/10.1134/S0021364013180136 (2013).
49. Valakh, M. Y. et al. Raman scattering and disorder effect in Cu_2ZnSnS_4. *Phys. Status Solidi RRL* **7**, 258–261. https://doi.org/10.1002/pssr.201307073 (2013).
50. Paris, M., Choubrac, L., Lafond, A., Guillot-Deudon, C. & Jobic, S. Solid-state NMR and Raman spectroscopy to address the local structure of defects and the tricky issue of the Cu/Zn disorder in Cu-Poor. *Zn-Rich CZTS Materials. Inorg. Chem.* **53**, 8646–8653. https://doi.org/10.1021/ic5012346 (2014).
51. Caballero, R. et al. Non-stoichiometry effect and disorder in Cu_2ZnSnS_4 thin films obtained by flash evaporation: Raman scattering investigation. *Acta Mater.* **65**, 412–417. https://doi.org/10.1016/j.actamat.2013.11.010 (2014).
52. Aroyo, M. I. et al. Bilbao crystallographic server: I. Databases and crystallographic computing programs. *Z. fur Krist. Cryst. Mater.* **221**, 15–27. https://doi.org/10.1524/zkri.2006.221.1.15 (2006).
53. Himmrich, M. & Haeuseler, H. Far infrared studies on stannite and wurtzstannite type compounds. *Spectrochim. Acta A* **47**, 933–942. https://doi.org/10.1016/0584-8539(91)80283-o (1991).
54. Fernandes, P. A., Salomé, P. M. P. & da Cunha, A. F. Study of polycrystalline Cu_2ZnSnS_4 films by Raman scattering. *J. Alloys Compd.* **509**, 7600–7606. https://doi.org/10.1016/j.jallcom.2011.04.097 (2011).
55. Dimitrievska, M. et al. Multiwavelength excitation Raman scattering study of polycrystalline kesterite Cu_2ZnSnS_4 thin films. *Appl. Phys. Lett.* **104**, 021901. https://doi.org/10.1063/1.4861593 (2014).
56. Kumar, M. & Persson, C. Cu_2ZnSnS_4 and $Cu_2ZnSnSe_4$ as potential earth-abundant thin-film absorber materials: a density functional theory study. *IJTAS.* **5**(1), 1–8 (2013).
57. Fairbrother, A. et al. Development of a selective chemical etch to improve the conversion efficiency of Zn-Rich Cu_2ZnSnS_4 solar cells. *J. Am. Chem. Soc.* **134**, 8018–8021. https://doi.org/10.1021/ja301373e (2012).
58. Darling, B. T. & Dennison, D. M. The water vapor molecule. *Phys. Rev.* **57**, 128–139. https://doi.org/10.1103/PhysRev.57.128 (1940).
59. Babichuk, I. S. et al. Raman mapping of MoS_2 at Cu_2ZnSnS_4/Mo interface in thin film. *Solar Energy* **205**, 154–160. https://doi.org/10.1016/j.solener.2020.05.043 (2020).
60. Dumcenco, D. & Huang, Y.-S. The vibrational properties study of kesterite Cu_2ZnSnS_4 single crystals by using polarization dependent Raman spectroscopy. *Opt. Mater.* **35**, 419–425. https://doi.org/10.1016/j.optmat.2012.09.031 (2013).
61. Guc, M. et al. Polarized Raman scattering study of kesterite type Cu_2ZnSnS_4 single crystals. *Sci. Rep.* **6**, 19414. https://doi.org/10.1038/srep19414 (2016).
62. Havryliuk, Y. et al. Raman characterization of Cu_2ZnSnS_4 nanocrystals: phonon confinement effect and formation of Cu_xS phases. *RSC Adv.* **8**, 30736–30746. https://doi.org/10.1039/c8ra05390a (2018).
63. Yaremko, A. M., Dzhagan, V. M., Yukhymchuk, V. O., Baran, J. & Ratajczak, H. Raman scattering in crystal multilayer structures with quantum dots: Theoretical and experimental study. *Superlattices Microstruct.* **48**, 85–105. https://doi.org/10.1016/j.spmi.2010.05.002 (2010).
64. Babichuk, I. S. et al. Spectroscopy and theoretical modeling of phonon vibration modes and band gap energy of $Cu_2ZnSn(S_xSe_{1-x})_4$ bulk crystals and thin films. *ACS Omega* **6**, 29137–29148. https://doi.org/10.1021/acsomega.1c04356 (2021).
65. Babichuk, I. S. et al. Control of secondary phases and disorder degree in Cu_2ZnSnS_4 films by sulfurization at varied subatmospheric pressures. *Sol. Energy Mater. Sol. Cells* **200**, 109915. https://doi.org/10.1016/j.solmat.2019.109915 (2019).
66. Sheleg, A. U. et al. Crystallographic and optical characteristics of thin films of $Cu_2ZnSn(S_xSe_{1-x})_4$ solid solutions. *J. Appl. Spectrosc.* **81**, 776–781. https://doi.org/10.1007/s10812-014-0005-8 (2014).
67. Fuhrmann, D., Dietrich, S. & Krautscheid, H. Zinc tin chalcogenide complexes and their evaluation as molecular precursors for Cu_2ZnSnS_4 (CZTS) and $Cu_2ZnSnSe_4$ (CZTSe). *Inorg. Chem.* **56**, 13123–13131. https://doi.org/10.1021/acs.inorgchem.7b01697 (2017).
68. Pogue, E. A., Sutrisno, A., Johnson, N. E., Shoemaker, D. P. & Rockett, A. A. Oxygen-induced ordering in bulk polycrystalline Cu_2ZnSnS_4 by Sn removal. *Inorg. Chem.* **56**, 12328–12336. https://doi.org/10.1021/acs.inorgchem.7b01777 (2017).
69. Golovynskyi, S. et al. Color manipulation of mechanoluminescence and photoluminescence from CaZnOS:ZnS:Mn^{2+} heterocompound controlled by ion doping concentration. *J. Alloys Compd.* **990**, 174437. https://doi.org/10.1016/j.jallcom.2024.174437 (2024).
70. Babichuk, I. S. et al. Thickness-dependent structural parameters of kesterite $Cu_2ZnSnSe_4$ thin films for solar cell absorbers. *Mater. Lett.* **225**, 82–84. https://doi.org/10.1016/j.matlet.2018.04.109 (2018).
71. Semenenko, M. O. et al. RF electromagnetic field treatment of tetragonal kesterite CZTSSe light absorbers. *Nanoscale Res. Lett.* **12**, 408–415. https://doi.org/10.1186/s11671-017-2183-9 (2017).
72. Babichuk, I. S. et al. Influence of hydrogen plasma treatment on secondary phases in CZTS thin films for energy harvesting. *Mater. Today Commun.* **28**, 102664. https://doi.org/10.1016/j.mtcomm.2021.102664 (2021).
73. Dzhagan, V. et al. Core and shell contributions to the phonon spectra of CdTe/CdS quantum dots. *Nanomaterials* **13**, 921. https://doi.org/10.3390/nano13050921 (2023).
74. Babichuk, I. S. et al. Optical and morphological properties of tetragonal Cu_2ZnSnS_4 thin films grown from sulphide precursors at lower temperatures. *SPQEO* **17**, 291–294, https://doi.org/10.15407/spqeo17.03 (2014).
75. Brus, V. V. et al. Raman spectroscopy of Cu-Sn-S ternary compound thin films prepared by the low-cost spray-pyrolysis technique. *Appl. Optics* **55**, B158. https://doi.org/10.1364/ao.55.00b158 (2016).
76. Matyash, I. E., Minailova, I. A., Serdega, B. K. & Babichuk, I. S. Research of optical and mechanical properties of lithium aluminosilicate glass-ceramics. *J. Non. Cryst. Solids* **459**, 94–98. https://doi.org/10.1016/j.jnoncrysol.2016.12.039 (2017).
77. Chen, W. et al. Improving the Strain control performance of MoS_2 monolayer to develop flexible electronics. *Adv. Eng. Mater.* **26**, 2301470. https://doi.org/10.1002/adem.202301470 (2023).
78. He, Z. et al. Flexible piezoelectric sensors based on ionic liquid-doped poly(L-lactic acid) for human coughing recognition. *Adv. Mater. Technol.* **9**, 2400386. https://doi.org/10.1002/admt.202400386 (2024).
79. Liu, Y. et al. A poly(L-lactic Acid)-based flexible piezoelectric energy harvester with micro-zigzag structures. *Smart Mater. Struct.* **33**, 075024. https://doi.org/10.1088/1361-665X/ad4e21 (2024).
80. Semenenko, M. et al. Red-shifted photoluminescence and gamma irradiation stability of "micromorph" (nc-Si/SiO)/DLC down-converter anti-reflection coatings. *Diam. Relat. Mater.* **100**, 107578. https://doi.org/10.1016/j.diamond.2019.107578 (2019).
81. Perdew, J. P., Burke, K. & Ernzerhof, M. Generalized gradient approximation made simple. *Phys. Rev. Lett.* **77**, 3865–3868. https://doi.org/10.1103/PhysRevLett.77.3865 (1996).
82. Monkhorst, H. J. & Pack, J. D. Special points for Brillouin-zone integrations. *Phys. Rev. B* **13**, 5188–5192. https://doi.org/10.1103/PhysRevB.13.5188 (1976).
83. Giannozzi, P. et al. QUANTUM ESPRESSO: a modular and open-source software project for quantum simulations of materials. *J. Phys. Condens. Matter.* **21**, 395502. https://doi.org/10.1088/0953-8984/21/39/395502 (2009).
84. Yaremko, A. M. et al. Many particle approach to resonance Raman scattering in crystals: Strong electron-phonon interaction and multi-phonon processes. *Chem. Phys.* **388**, 57–68. https://doi.org/10.1016/j.chemphys.2011.07.023 (2011).

85. Nishiwaki, M. et al. Tail state formation in solar cell materials: First principles analyses of zincblende, chalcopyrite, kesterite, and hybrid perovskite crystals. *Phys. Rev. Mater.* **2**, 085404. https://doi.org/10.1103/PhysRevMaterials.2.085404 (2018).

Author contributions

Y.A. R., I.S. B. conceptualization, data curation, formal analysis, investigation, visualization, and writing (review & editing). V.O. Y., V.M. D. formal analysis, investigation, writing (review & editing). V.V. K., S.V. V., M.O. S., M.O. St., A. T., L.M. P, D. L. formal analysis, software, methodology, visualization, writing (review & editing), funding acquisition.

Funding

This research was supported by Project FONDECYT (1240985), Centers of Excellence with BASAL/ANID financing (AFB220001), the Innovation Program for Quantum Science and Technology (2023ZD0300300), Key-Area Research and Development Program of Guangdong Province (2020B0101030002), and in part by Wuyi University-Hong Kong-Macao Joint Research Funds (2019WGALH19).

Declarations

Competing interests

The authors declare no competing interests.

Additional information

Supplementary Information The online version contains supplementary material available at https://doi.org/10.1038/s41598-024-83117-9.

Correspondence and requests for materials should be addressed to Y.A.R., I.S.B. or A.T.